



Grant Agreement No: 101004761

AIDAinnova

Advancement and Innovation for Detectors at Accelerators
Horizon 2020 Research Infrastructures project AIDAINNOVA

MILESTONE REPORT

IDENTIFICATION OF A GAS MIXTURE FOR NEUTRINO PHYSICS IN AN OPTICAL TPC

MILESTONE: MS27

Document identifier:	AIDAinnova-MS27
Due date of milestone:	March 2024
Report release date:	09/04/2023
Work package:	WP7: Gaseous Detectors
Lead beneficiary:	IGFAE/IFIC
Document status:	Final

Abstract:

Next-generation megawatt-scale neutrino beams open the way to studying neutrino-nucleus scattering resorting, for the first time, to gaseous targets. This represents an opportunity to improve the knowledge of neutrino cross sections in the energy region between hundreds of MeV and a few GeV, of interest for the upcoming generation of long-baseline neutrino oscillation experiments. The challenge is to accurately track and (especially) time the particles produced in neutrino interactions in large and seamless volumes down to few-MeV energies. We propose to accomplish this through an optically-read Time Projection Chamber (TPC) filled with high-pressure argon and equipped with both tracking and timing functions. In this work, we present a detailed study of the time-tagging capabilities of such a device, based on end-to-end optical simulations that include the effect of photon propagation, photosensor response, dark-count rate and pulse reconstruction. We show that the neutrino interaction time could be reconstructed from the primary-scintillation signal with a precision in the range 1-2.5 ns (σ) for point-like deposits with energies down to 5 MeV, and well below 1 ns for minimum-ionizing particle tracks. A discussion on previous limitations towards such a detection technology, and how they can be realistically overcome in the near future thanks to recent developments in the field, is presented (particularly the strong scintillation yields recently reported for Ar/CF₄ mixtures). The performance presented in our analysis seems to be well within reach of next-generation neutrino-oscillation experiments through the instrumentation of the proposed TPC with conventional reflective materials and a SiPM carpet behind a transparent cathode.

AIDAinnova Consortium, 2024

For more information on AIDAinnova, its partners and contributors please see <http://aidainnova.web.cern.ch/>

The Advancement and Innovation for Detectors at Accelerators (AIDAinnova) project has received funding from the European Union's Horizon 2020 Research and Innovation programme under Grant Agreement no. 101004761. AIDAinnova began in April 2021 and will run for 4 years.

Delivery Slip

	Name	Partner	Date
Authored by	D. González-Díaz J. Martín-Albo Simón	IGFAE IFIC	17/03/2024
Edited by	D. González-Díaz	IGFAE	17/03/2024
Reviewed by	S. Dalla Tore [WP Coordinator] B. Schmidt [WP Coordinator]	INFN CERN	30/03/2024
Approved by	P. Giacomelli [Scientific coordinator] Steering Committee	INFN	09/04/2024

TABLE OF CONTENTS

1. INTRODUCTION	4
2. EXPERIMENTAL RESULTS.....	7
2.1. PRIMARY SCINTILLATION.....	7
2.2. SECONDARY SCINTILLATION AND MUON TRACKING	10
2.3. SIMULATED PERFORMANCE IN A LARGE-VOLUME ARGON TPCS.....	12
3. TECHNOLOGICAL ASSETS	16
3.1. ACTIVE SIPM GANGING.....	16
3.2. ACTIVE CRYOSTAT.....	18
3.3. IMPACT OF TEFLON REFLECTOR ON TPC PERFORMANCE	20
4. CONCLUSIONS AND OUTLOOK	21
5. REFERENCES	22

Executive summary

*This document contains the demonstration of the main enabling assets (as well as a viable roadmap) towards the implementation of a “Full3D Optical TPC” for the study of Neutrino Interactions in next-generation TPCs. This means: to provide accurate timing and tracking of the particles emerging from primary neutrino interactions, by optical means. It thus expands over the original motivation, that was to identify a gas mixture compatible with time tagging (i.e., primary scintillation -sensitivity). Our work focuses on **Argon** as the main gas, with a suitable molecular additive at low concentration acting as wavelength-shifter, given that the most obvious application of the technology is the DUNE experiment. Questions remain on whether this approach can be ported to other gaseous targets and, although the answer is not straightforward and requires experimental validation, the prospects to extend this concept beyond the proposed application are intriguing.*

1. INTRODUCTION

The *Time Projection Chamber* (TPC) has been at the forefront of particle physics research for the last four decades, finding numerous applications in areas ranging from heavy-ion physics to rare-event searches. In neutrino physics, the liquid argon TPC (LArTPC), originally proposed in the late 1970s, is now the cornerstone detector technology of the short- and long- baseline neutrino oscillation programs under development in the United States. More recently, magnetized Gaseous Argon TPCs (GARTPCs) have also been proposed as neutrino detectors [1,2]. Their combination of high-resolution tracking, ability to reconstruct short hadron tracks down to a few MeV, and powerful particle identification through dE/dx would help improve our knowledge of neutrino-nucleus scattering in the few-GeV region, reducing systematic errors in the new generation of neutrino oscillation experiments.

A key aspect of the design of a GARTPC is that, in contrast to the liquid phase, high-resolution tracking in pure argon gas is not viable due to: i) high electron diffusion, and ii) low primary ionization per mm combined with a very low avalanche amplification factor (around 15-30 e^-/e^-), [3,4,5]. Illustratively, at 10 bar and for a typical drift field of 400 V/cm, the ionization spread resulting from a 5 m drift would be 2.2 cm (transverse) and 0.8 cm (longitudinal). Such diffusion values are more than one order of magnitude higher than those usually found in state-of-the-art gaseous TPCs, while the gain is at least 100 times lower. Electron diffusion can be greatly reduced through the addition of a small fraction of a molecular gas (typically, at the few-percent level or above). This helps as well with the stabilization of the avalanche process by absorbing the very energetic scintillation photons emitted by rare gases as well as quenching its emission.

The above creates an apparent technological dilemma: in a GARTPC, good tracking capabilities and usable levels of scintillation seem to be incompatible. In the LArTPCs used as neutrino detectors, the primary-scintillation signal provides the absolute timing of the recorded tracks, which is required to disambiguate their position along the drift direction. In a GARTPC, although one could in principle rely on external instrumentation to time those neutrino interactions through tracks escaping the TPC, that would leave unreconstructed the 3D position of many reactions of interest. Even in the gaseous phase, tracks of up to 100-200 MeV may range-out inside the TPC depending on the conditions (see Fig. 1). In other words, the main advantage of a GARTPC, its ability to reconstruct low-energy interactions, would be hindered by its inability to time-tag them.

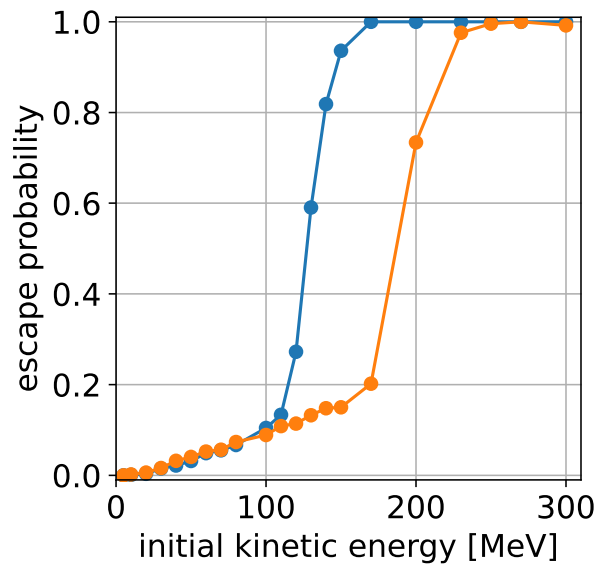


Fig. 1 Escape probability (estimated with Geant4) of protons from a cylindrical TPC 5 m in diameter and 5 m long housed in a high-pressure steel vessel filled with filled with Ar/CF₄ (99/1) at 10 bar. The blue data correspond to a 1-cm-thick vessel; the orange data, to a 3-cm-thick one. Protons were generated isotropically from the center of the detector.

An appealing path forward is to induce wavelength shifting of the argon scintillation directly in the gas, as this process can simultaneously remove the avalanche-destabilizing vacuum-ultraviolet (VUV) photons from argon, while preserving a significant fraction of the scintillation yield. One can anticipate additional advantages like easier light collection and detection away from the VUV, or a faster time response (given the very long time constant of 3.2 μ s from the Ar₂^{*} triplet state, responsible for about 80-90% of the argon scintillation emission [6]). If gaseous wavelength-shifting can be accomplished through a molecular species, then the suppression of diffusion to manageable levels as well as the enhancement of the avalanche multiplication factor can be expected too.

Recently, high wavelength-shifting efficiency has been demonstrated for Ar/CF₄ mixtures [7,8], resulting, for a mere 1% volume fraction of CF₄, in scintillation strengths of about 1400 photons per MeV in the range between 400 and 700 nm (Fig. 2, top row). Such small additive concentrations are an important asset in order to avoid the contamination of the neutrino-Ar scattering data with spurious interactions from other nuclear species. Simulations performed with Pyboltz support the fact that, at 400 V/cm, the strong electron cooling of CF₄ would reduce transverse diffusion down to 3.6 mm for a drift length of 5 m (Fig 2, bottom-left), a value lower even than what can be achieved with standard gas mixtures such as Ar/CH₄ at 90/10 (P10), for which a spread of 4.0 mm is expected. According to Pyboltz, this performance is preserved in a wide range of drift fields (tens of V/cm/bar, in a pressure-reduced representation). Although information on avalanche gain for low-quenched Ar/CF₄ mixtures is scarce, values in excess of 10⁴ have been reported in single-wire configuration [9], and around 3 x 10⁵ in 3-GEM stacks down to CF₄ concentrations as low as 2% at around atmospheric pressure [10]. The latter detector, instrumenting an area of 10x10 cm², provided high-quality α [11,12] and X-ray [13] images with reliable performance over the course of years, and is still in use at CERN's Gas Detectors Development laboratory. More recently, muon tracks have been imaged in Ar/CF₄ (99/1) at 1 bar by resorting to a double glass-THGEM stack [14], (Fig 2, bottom-right panel). The characteristics of CF₄ as a wavelength-shifting gas are convenient: it is relatively fast (most of the light is emitted with a time constant of about 15 ns, a feature preserved in the presence of Ar) and its emission spectrum lies largely in the near ultraviolet and visible regions, offering good prospects for detection. It is also highly immune to contaminants: at 1 bar, even a (certainly unrealistic) 3% N₂ contamination would cause a tolerable x2 reduction of the CF₄ scintillation strength [15].

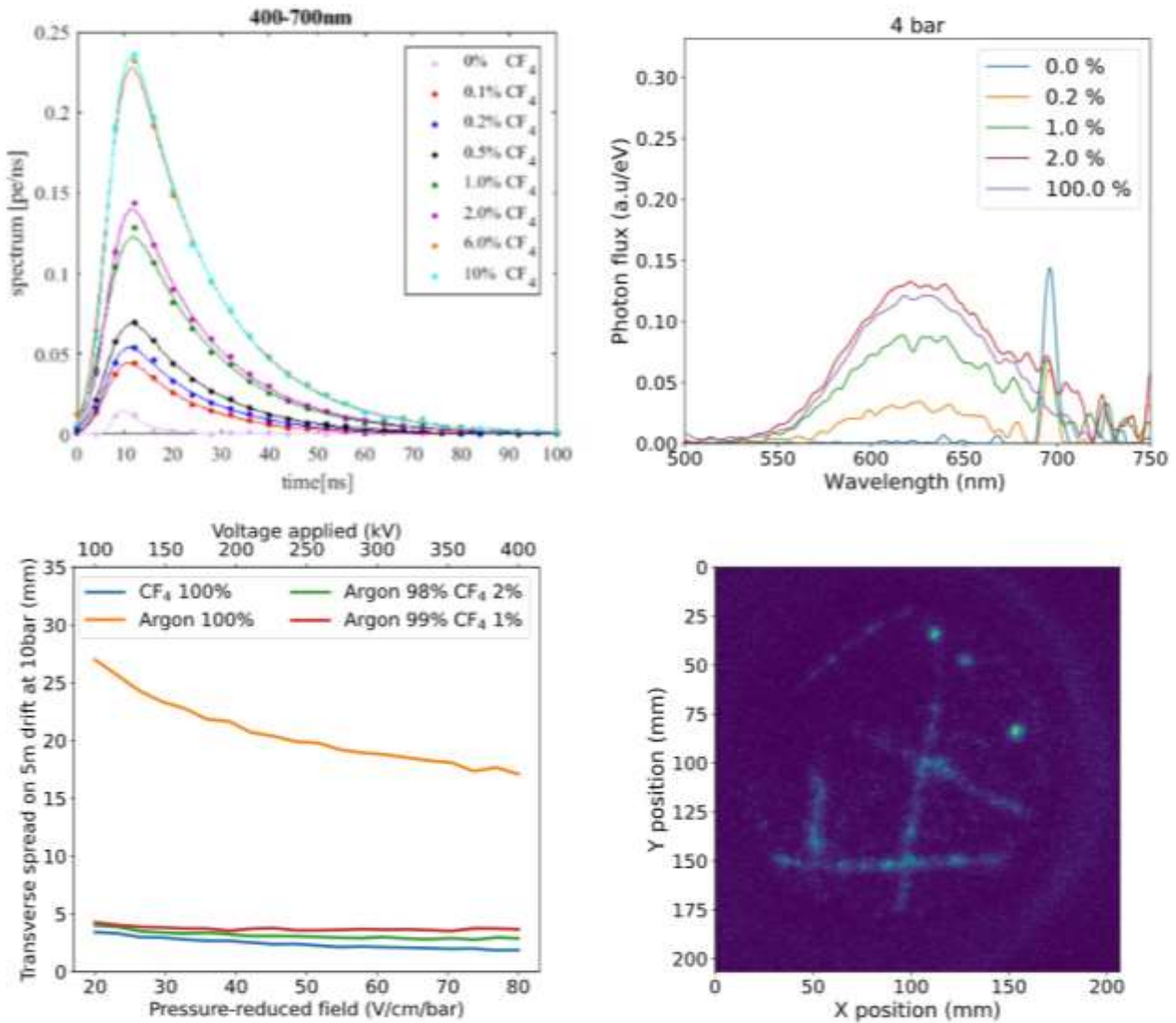


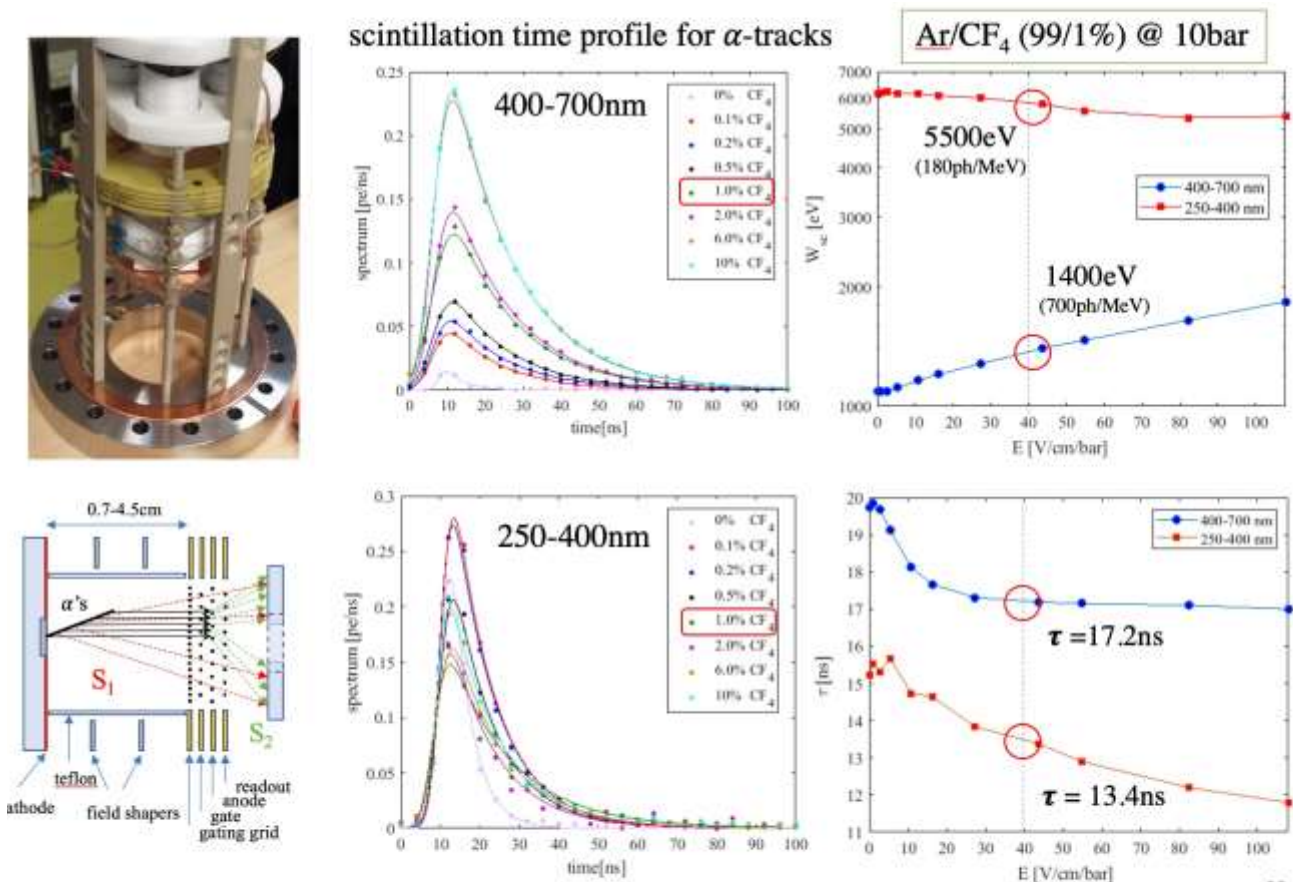
Fig. 2 Some fundamentals relevant to the present work. From top-left to bottom-right: (i) scintillation time profiles under 5.5 MeV α -particles for Ar/CF₄ mixtures at 10 bar (adapted from [8]); (ii) spectrum of emission of Ar/CF₄ in the visible region, per unit of energy deposited in the gas, obtained with an X-ray tube (adapted from [7]); (iii) transverse spread of the primary ionization after 5 m drift in different Ar and Ar/CF₄ mixtures, as obtained with Pyboltz [16]; (iv) cosmic ray tracks obtained in Ar/CF₄ (99/1) at 1 bar with a double-stack of glass-THGEMs [14].

Here we assess the potential of Ar/CF₄ mixtures for time-tagging in GARTPCs. The report is structured as follows: Section 2 describes the main experimental results as well as sensitivity simulations performed with Geant4, that validate the proposed technology. Section 3 contains a technical discussion on (i) the impact of the photosensor response, digitization scheme and electrical noise, as well as the progress made with active SiPM ganging and (ii) a simple proposal of an active cryostat aimed at achieving photosensor cooling in high-pressure closed systems, together with first experimental results validating the idea. A short discussion on the impact of the proposed Teflon reflector on the chamber performance can also be found in this section.

2. EXPERIMENTAL RESULTS

2.1. PRIMARY SCINTILLATION

Primary scintillation was measured in two consecutive campaigns, the first of them focused on the scintillation yields and time-resolved spectra, the second one on the spectroscopic response. For the yield measurements, the focus were the scintillation characteristics at 10 bar, under different additive concentrations. An α source was employed at the cathode of a purposely built mini-TPC, readout with MWPC chambers. The setup was identical to the one used in [17], that had been employed earlier in the detailed studies of xenon scintillation. The W_{sc}^1 -values obtained for xenon, based on a Geant4 analysis of the geometrical corrections yielded a value of the order of 40 eV, that agrees well, within less than 20%, with independent estimates. Measurements were performed as a function of the CF_4 concentration and the electric field, and the results can be found in Fig. 3. Scintillation yields in the visible range amount to 1400 photoelectrons/MeV at around 40 V/cm/bar (the figure displays 700 photoelectrons/MeV, a value coming from a preliminary PM calibration) and considerably lower yields are observed in the UV range. The dependence with the field is reminiscent of charge-recombination, an effect reported earlier in pure CF_4 . Decay time constants are very short, much shorter than those involved in Ar scintillation, and thus provide a direct hint to the fact that emission may happen through wavelength shifting.



¹ W_{sc} refers to the energy needed to create a scintillation photon (in a given band) and is defined by analogy with the W_I value (the energy to create an electron-ion pair). Its inverse is the scintillation yield (defined in units of photoelectrons/MeV).

Fig. 3 Experimental setup used to measure primary scintillation in Ar/CF₄ mixtures at 10 bar. The setup consists of 4PMs, two of which have UV and visible filters (Note: the blue line in Fig. up-right has changed by a factor x2 after a detailed assessment of the single-photon calibration, providing the result used hereafter, in particular in section 2.3).

A complementary measurement was performed with an X-ray tube, utilizing the setup in Fig. 4 (and described in detail in [7]). Special care was taken of excluding effects like space-charge and charge-recombination. Fig. 5 shows the results for pure gases and comparisons with existing data. Fig. 6 shows the compilation of the complete experimental systematics, performed in the range of CF₄ concentrations from 0.1% to 10%, and pressures from 1 to 5 bar.

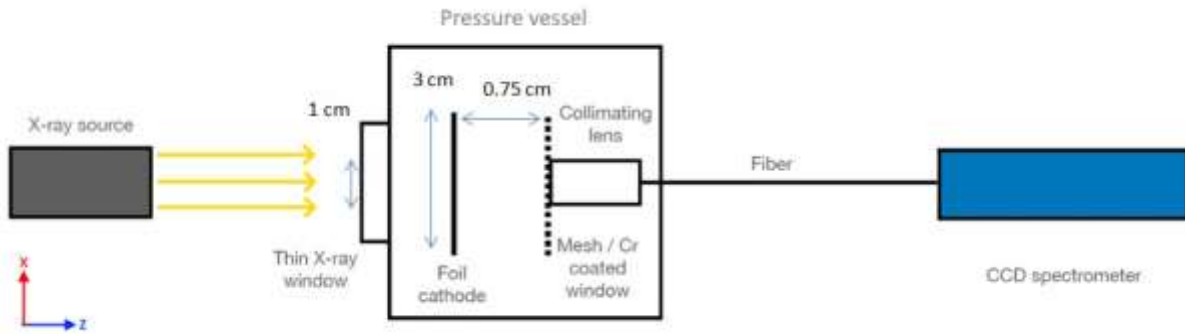


Fig. 4 Schematic drawing of the experimental setup used to conduct the measurements. The x-ray tube is shown to the left, the high-pressure vessel housing the electrifiable scintillating cylinder is shown at the middle. The spectrophotometer is shown to the right.

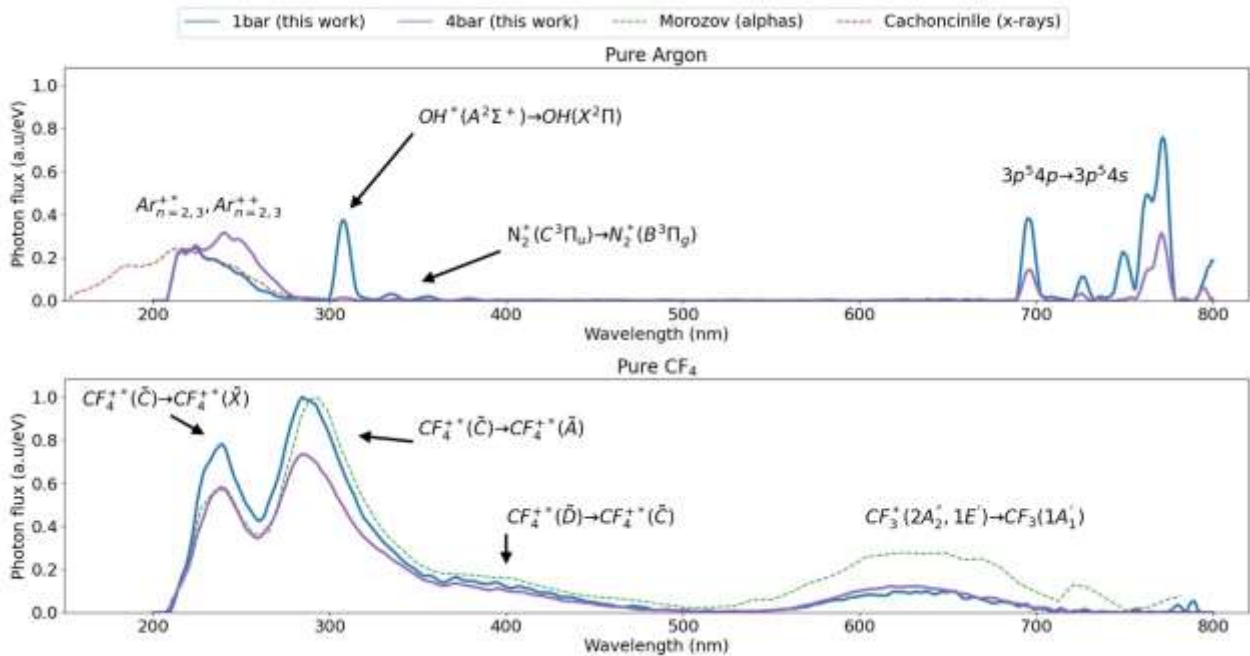


Fig. 5 Emission spectra per eV of released energy for pure argon (upper plot) and pure CF₄ (lower plot) at 1 and 4 bar (blue, purple), obtained at zero field. No significant dependence with the intensity of the X-ray tube was observed, suggesting that measurements are recombination-free. For pure CF₄, where full charge collection could be reached before the onset of secondary scintillation, no dependence with the electric field was observed either. The spectra of argon's 3rd continuum obtained in the work of Cachoncille [18] also with X-rays (red-dashed) and the one of CF₄ obtained by Morozov [19] with α -particles (green-dashed) are shown for comparison. A global normalization was imposed by setting to 1 the maximum of the 290 nm peak in pure CF₄ at 1 bar.

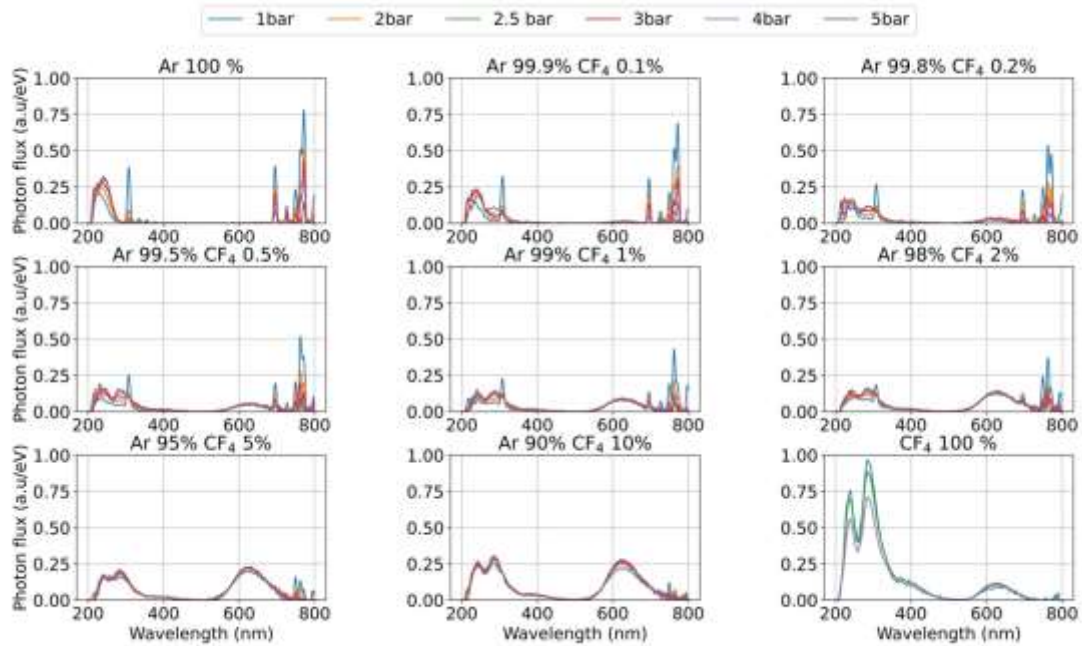


Fig. 6 Emission spectra per eV of released energy for different concentrations of Ar/CF₄, at zero field. Measurements are expected to be free from recombination effects, as discussed in text. A global normalization was imposed by setting to 1 the maximum of the 290 nm peak in pure CF₄ at 1 bar.

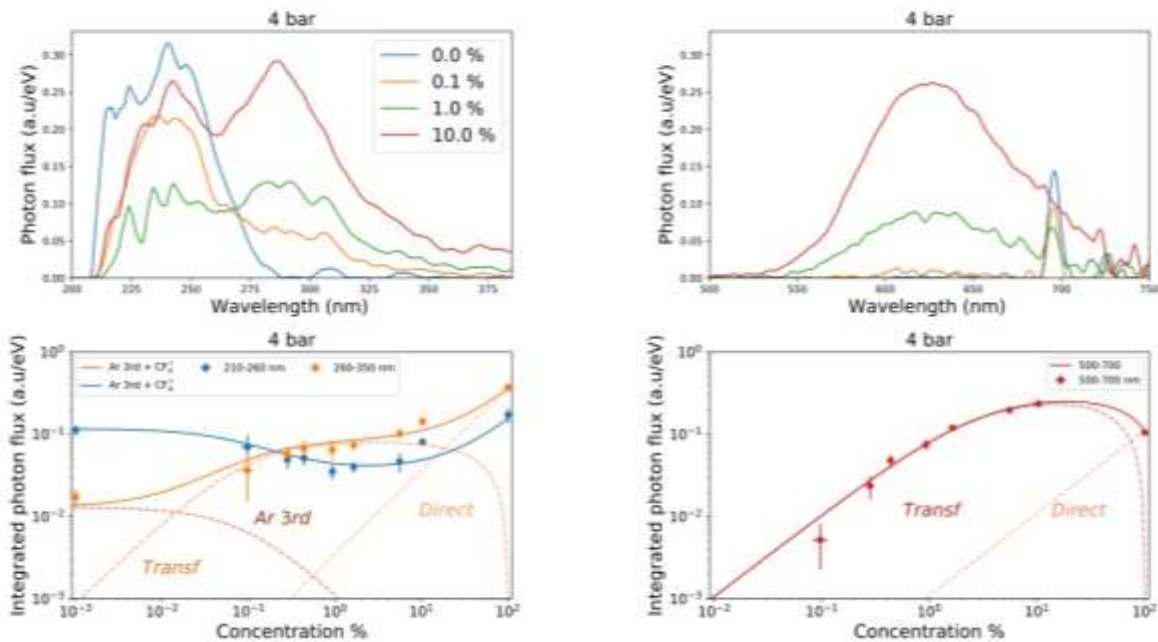


Fig. 7 Top row: scintillation spectra for different CF₄ concentrations at 4 bar, zoomed in the ultraviolet (left) and visible (right) regions. Bottom row: integrated yields on the ultraviolet (left) and visible (right) regions (shown as closed circles), superimposed to the kinetic model introduced in text. The experimental value for zero concentration is added on the bottom-left plot at 0.001% CF₄, taking advantage of the fact that the model asymptotically tends to a constant in that case.

Fig. 7 shows the scintillation yields and comparisons with a 2-parameter model (per band) that successfully describes the observations. The results show, with little ambiguity, that the 3rd continuum precursors of argon are responsible for the transfers to the CF₄⁺ precursors, ending in the UV

emission. The visible scintillation has been attributed to an intermediate Ar^{**} or Ar/CF_3^* exciplex, but its nature still needs to be elucidated through independent measurements. The spectroscopic work confirms the strong wavelength-shifting of the Ar/CF_4 system, with as much scintillation for 1% as for 100%, in the visible range. Remarkable properties of the mixtures, that extend to lower pressures (although not reported here), are the large pressure-independence of the yields (specially on the visible band), down to 10's of mbar.

2.3 SECONDARY SCINTILLATION AND MUON TRACKING

The experimental setup consisted in this case of a cylindrical field cage housed within a 40 litre ultra-high vacuum (UHV) vessel (Fig. 8). An Andor iXon Ultra 897 EMCCD camera with a Spacecom VF50095M lens was mounted on top of the centrally positioned DN 100 CF upper flange of the vessel. This top port was surrounded symmetrically by four ports with DN 40 CF flanges, which allow the mounting of electric and gas feedthroughs. The pressure and vacuum levels were monitored through one of these with a MKS 974B-71024 QuadMag Vacuum Transducer. Inside the vessel, a collimated 5.5 MeV Am-241 alpha source with a rate of 200 Hz was suspended by a rotary feedthrough. This allowed us to generate alpha tracks in the active volume by rotating the source in, and to image cosmic muons by rotating it out. The electrons generated in these events were drifted to the top of the TPC by means of a constant electric field, created by a 19 cm-long field cage. Facing this field cage, at the very bottom of the setup, there was an 8-inch Hamamatsu R5912-02MOD PMT. At the top of the field cage, two glass-THGEMs with holes of diameter 0.5 mm and pitch 0.8 mm were installed, separated by a transfer gap of 5 mm. The substrate (1 mm thick) of the bottom THGEM was made from Schott Borofloat 33, whilst that of the top THGEM was from fused silica. In both cases, the electrodes were made from an indium tin oxide (ITO) coating on the substrate.

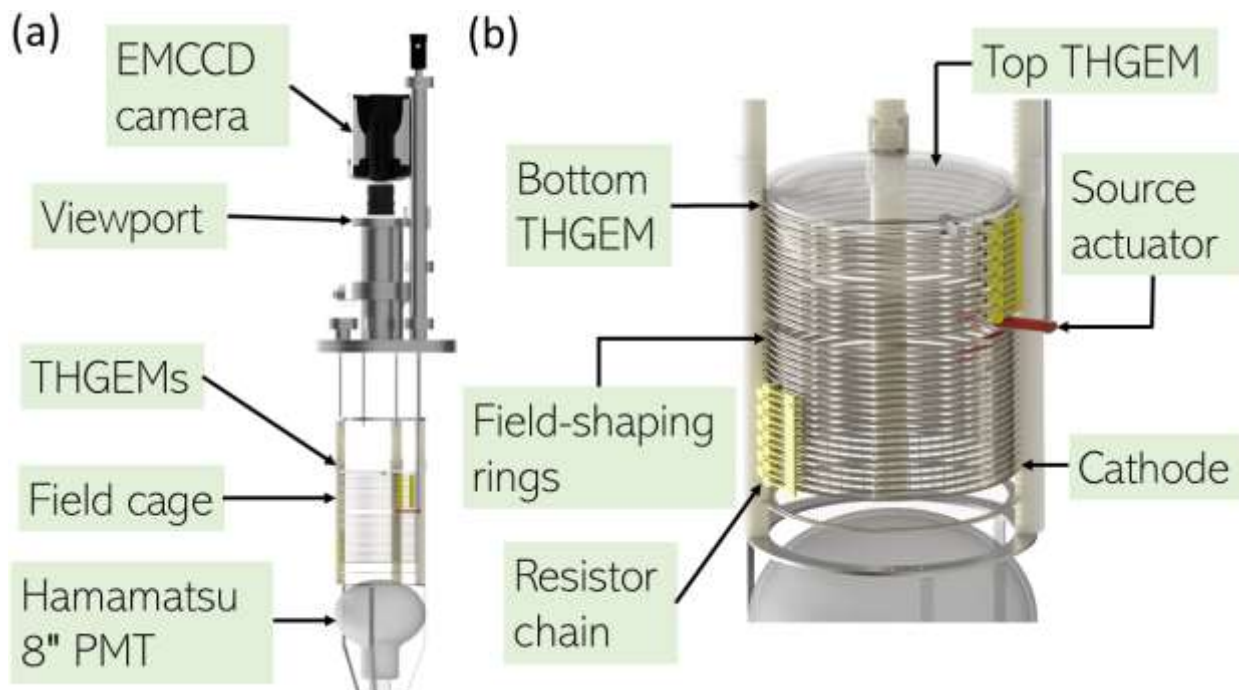


Fig. 8 A 3D CAD design showing (a) the main components of the detector and (b) a closer view of the field cage region (courtesy of A. Roberts, University of Liverpool).

In order to characterize the optical gain as a function of the voltage applied to the THGEMs, EMCCD data were collected with a long exposure time using an alpha source. When the bottom THGEM was operated, the top one had no electric field applied. In contrast, when the top THGEM was operated,

the bottom one had a small electric field to ensure a good electron transmission. In both cases, the background was characterized thoroughly to eliminate any possible light contamination. The reduced drift field and transfer field between both THGEMs was 0.1 kV/cm/bar and 1 kV/cm/bar respectively, for all measurements.

Once both THGEMs had been characterized, the alpha source was removed in order to collect data from cosmic rays. In this case, both THGEMs were biased simultaneously up to the highest voltage they were able to sustain before discharging. The breakdown voltage was typically higher than the one obtained for alphas, which is to be expected based on the higher ionization density and rate of the alpha source.

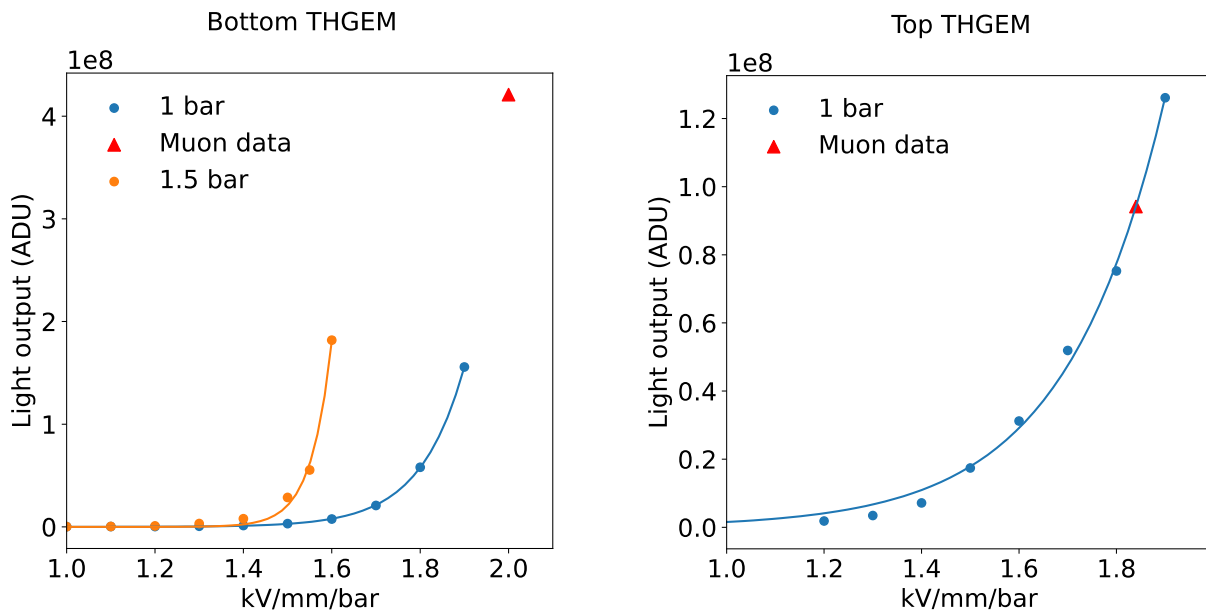


Fig. 9 Light output from the EMCCD camera (ADU) for bottom and top THGEMs at 1 bar (blue) and 1.5 bar (orange) in Ar/CF₄ (99/1), as a function of the pressure-reduced electric field across the THGEMs (background light at zero field has been subtracted). The solid lines represent exponential fits to the experimental data. The extrapolation/interpolation (red triangles) of the light output for the conditions at which muon data were taken, that is, 1.84 kV/mm/bar for the top THGEM and 2 kV/mm/bar for the bottom THGEM, is also displayed. No sizeable deterioration of the maximum gain was observed under a modest 50% increase in pressure. The pressure was limited by the experimental setup.

The integrated light intensity in the alpha-irradiated region of the images from the EMCCD camera can be studied as a function of voltage, for both THGEMs (Fig 9). The optical gain (at the point of production) was estimated from the following formula:

$$\text{gain}_{\text{ph}} = n_{\text{ph}} \cdot W_i / (\text{GE} \cdot \text{QE} \cdot E_{\alpha} \cdot f_{\alpha} \cdot t_{\text{exp}})$$

by resorting to the following magnitudes: the quantum efficiency (QE) of the EMCCD camera, the geometrical efficiency of the setup (GE), the W_i value of the mixture, the exposure time (t_{exp}) and the rate (f_{α}) and energy (E_{α}) of the Am-241 alpha source. In this case, the GE was assumed to be given by the solid angle subtended by the lens at the object plane and the QE was taken from the manual. When the bottom THGEM was studied, a transparency factor of 75% was considered. Estimates for bottom and top THGEMs using this method provided a maximum optical gain of the order of 10^3 (photoelectrons/e) for each of them.

Once the alpha source had been removed from the setup, data from cosmic rays were taken. A selection of different events with varying track topologies can be seen in Fig. 10.

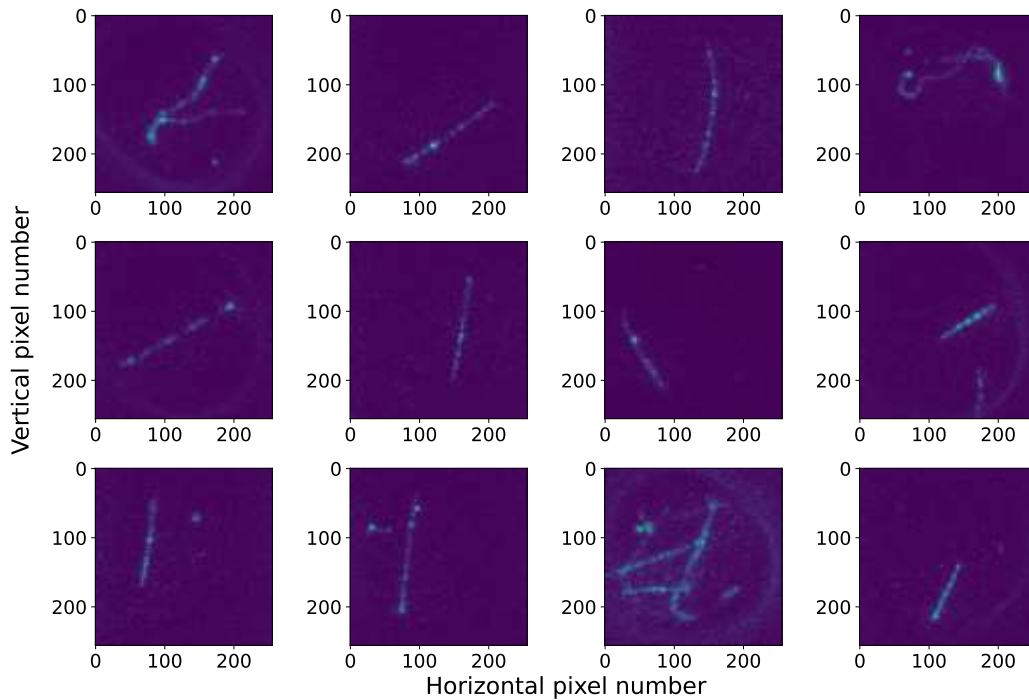


Fig. 10 Gallery of cosmic rays at 1 bar in Argon (1% CF_4 doping). The working fields were 1.84 kV/mm/bar for the top THGEM and 2 kV/mm/bar for the bottom THGEM. The exposure time was 0.1 s in all cases and the EMCCD gain was set to 1000.

2.4 SIMULATED PERFORMANCE IN A LARGE-VOLUME ARGON TPC

(The results in this section are greatly expanded in [20]). There are, in principle, several large-area photosensors that could be suitable for the task proposed, including Photomultiplier Tubes (PMTs), Microchannel Plates (MCPs), Avalanche Photodiodes (APDs), CMOS or CCD cameras, and Silicon Photomultipliers (SiPMs). Examination of the main technical caveats seem to favour one of these options, as long as the discussion is restricted to demonstrated technological solutions:

- **PMTs:** when it comes to large aperture, there is currently no commercial PMT above 1 inch that is rated for 10 bar. Moreover, ensuring magnetic-field compatibility inside the intended 0.5 T field would require dedicated R&D. Last, the quantum efficiency (QE) of vacuum photocathodes in the red region of the spectrum is largely below what is achievable with silicon devices and sits generally below 10%.
- **MCPs:** compared to PMTs, microchannel plates have better immunity to magnetic fields, but they suffer too from the lack of availability of high-pressure devices and low QE in the visible range, as PMTs do. For both PMTs and MCPs, detection of the UV-component of Ar/ CF_4 might offer a better alternative in case of vacuum photocathodes but remains to be studied.
- **APDs:** in the present concept the scintillation will be generally down to single-photon levels per sensor, thus making this option non-viable.
- **CMOS or CCD cameras:** with a QE as high as 70% or more in the visible spectrum and coupled to suitable optics, they can image large areas; however, they cannot be realistically used for the small signals expected in our case (hundreds of photoelectrons over the entire readout plane) due to simple solid-angle considerations.
- **SiPMs:** they can operate under high pressure and high magnetic fields, and their quantum efficiency can reach 30% at 600 nm. Historically, SiPMs have suffered from high dark count rate (DCR); however, improvements over the last decade brought it down to the level of 50-

100 kHz/mm² at room temperature, with ongoing efforts to bring it even further down. SiPMs are typically small, and hence not optimal for large-area coverage unless several channels can be combined. Their large gain facilitates this process, and signal-to-noise ratios better than 10 have been achieved, for instance, ganging together twenty-four 10 x 10 mm² SiPMs [21].

In summary, an array of SiPMs tiling the cathode could, realistically, instrument the proposed TPC as long as the photosensors' DCR can be kept at tolerable levels. A common solution involves operation at low temperature, as the DCR is reduced by about an order of magnitude every 25° C. As shown, temperatures around 25° C seem sufficient, in our case, for achieving the target performance. These moderately-low local temperatures are not unknown to particle physics instrumentation, even with the rest of the detector operating comfortably at room temperature (e.g., [22]). Ongoing studies point to the fact that two PMMA windows - one at the cathode and another one next to the photosensors - would suffice at providing thermal insulation between the active volume of the TPC and the SiPM plane, keeping the cooling power at reasonable levels. For the evaluation of the detector performance, we consider as a prospective SiPM the 14160/14161 series by Hamamatsu, with a photosensor arrangement in square tiles of 35 x 35 cm² at a pitch of 40 cm, leading to a maximum fill factor of 76.5%. The additional 5 cm provides space for the frames of the cryostat assembly, greatly reducing the thermal stress on the PMMA window. Conservatively, the reference simulations presented here have been done for half of the maximum fill-factor estimated this way (i.e., 38%, 7.5m² photosensor area).

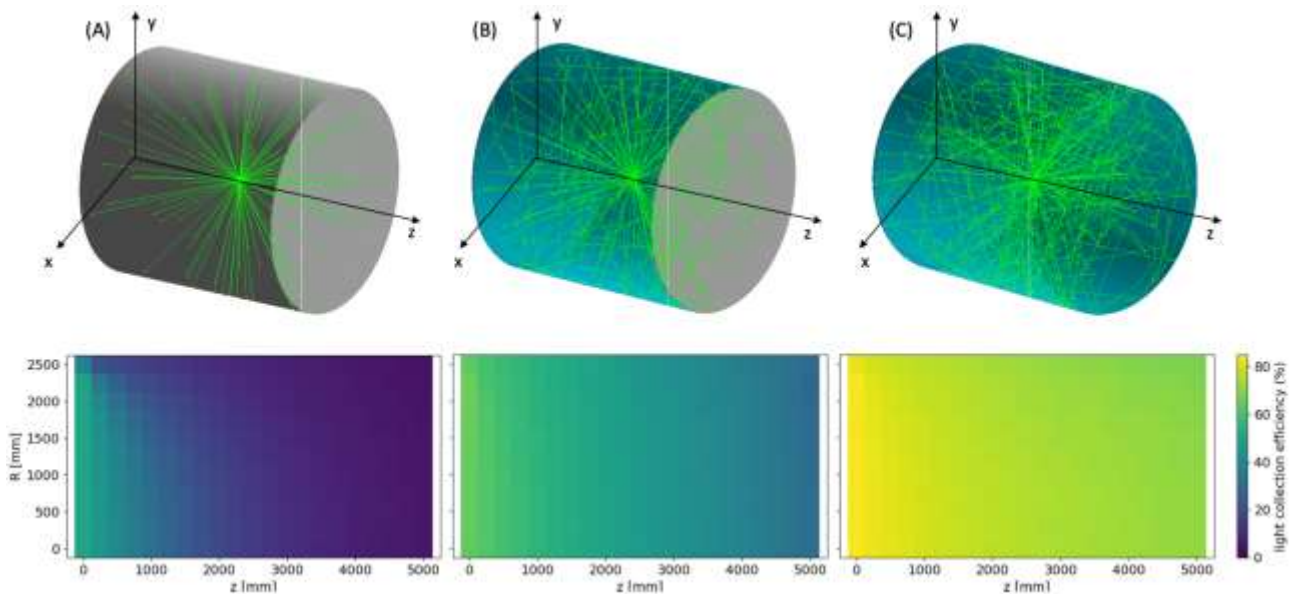


Fig. 11 Results from photon tracing for the three TPC configurations discussed, where reflective surfaces are represented in blue and non-reflective ones in grey: (A) TPC without reflective lining; (B) TPC with a PTFE reflector covering the interior of the field cage; and (C) like case B, but with aluminized GEMs instrumenting the anode. The plots on the second row show the light collection efficiency as a function of the radial and axial positions of a point-source for each of the configurations. The axial coordinate z is taken to be zero at the photosensor plane.

We evaluated the expected performance of the TPC concept described above by means of a Geant4 end-to-end simulation that covers from the generation and transport of particles interacting in the detector, to the production of the primary scintillation photons (and ionization electrons), and, finally, their tracing (collection), amplification and conversion into electric signals. It implements a detailed optical model of the TPC geometry, for which we will consider three main configurations (see Fig. 11, top row): (A) no reflectors; (B) a PTFE-lined field cage (with exposed field shapers, to minimize

charging-up) and a fully absorbing anode; (C) a PTFE-lined field cage and an anode based on aluminized GEMs. The TPC is 5 m in diameter and 5 m long in the axial dimension.

Using our Geant4 simulation, we computed the light collection efficiency (η) of the detector, defined as the number of photons reaching the photosensors (i.e., excluding their photon detection efficiency) divided by the number of generated ones. It is shown as a function of cylindrical coordinates (radial and axial position) in Fig. 11 for the three TPC configurations listed above. To simplify the discussion, Fig. 12 shows η for different positions of a point source placed along the central axis of the TPC. The collection efficiency decreases fast towards the anode (higher z) in the absence of reflectors (square data points), flattening when reflectors are included in the field cage (red circles) and at the anode (blue triangles). Differences in η obtained by replacing Teflon (a brand name for PTFE) with specular reflector film (ESR) - with average reflectance around 98% in our range of interest-, or using either large-pitch (LP) aluminized GEMs (dark blue triangles) or conventional standard-pitch (SP) ones (light blue triangles) are all well within 10 percentage points. Hence, without resorting to special techniques, light collection values in the range 70-90% may be reached over the entire chamber, showcasing the convenience of using visible light for detection.

The average number of photoelectrons (N_{pe}) expected from a physics signal is given, approximately, by the following expression:

$$N_{pe} \simeq Y_{sc} \cdot \eta \cdot T_{PMMA} \cdot T_{PMMA} \cdot F_{SiPM} \cdot \varepsilon_{SiPM}$$

where a light yield of $Y_{sc} = 1400$ photons/MeV has been established in section 2, for the visible range, in Ar/CF₄ (99/1) at 10 bar; η is the light collection efficiency; $T_{PMMA} \simeq 0.9 \cdot 0.9 = 0.81$ is the optical transmission of the two PMMA windows in front of the photosensors; $F_{SiPM} = 0.38$ is the fill factor of the SiPM array; $\varepsilon_{SiPM} = 0.255$ is the average photon detection efficiency (PDE) of the SiPMs in response to the visible component of Ar/CF₄. For a point-like event (e.g., a few MeV proton track) in the center of a Teflon-lined TPC (configuration B), $\eta = 47\%$ is obtained (red solid circles) and, hence:

$$N_{pe} \simeq 52 \text{ photoelectrons/MeV,}$$

ranging between 38 and 71 for events in the vicinity of anode and cathode, respectively.

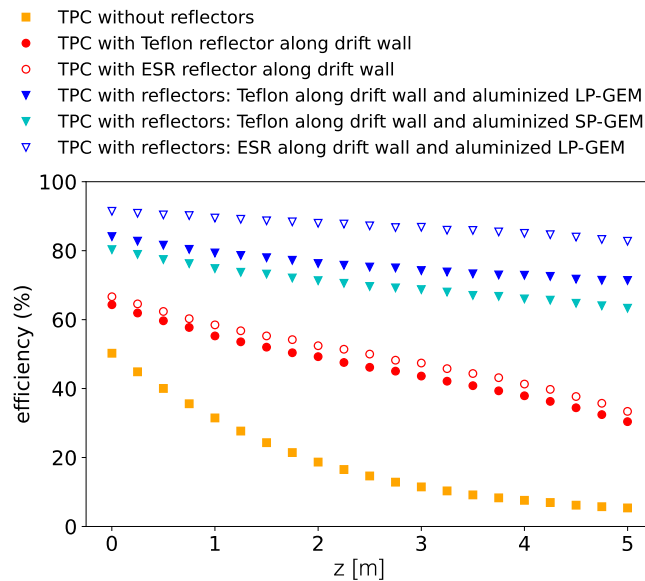


Fig. 12 Light collection efficiency (η) for the three main TPC configurations discussed in text: (A) TPC without reflective lining (orange squares); (B) TPC with Teflon (or ESR reflector) in the field cage (red symbols); (C) like case B, but with aluminized GEMs instrumenting the anode (blue symbols). The axial coordinate z is taken to be zero at the photosensor plane.

The minimum particle energy needed to enable detection of the primary scintillation signal can be estimated by defining the $5\text{-}\sigma$ sensitivity of the SiPM array as the average upper limit (computed here using the Feldman-Cousins frequentist prescription) that would be obtained by an ensemble of measurements with the expected background (the photosensor's DCR) and no true signal. Figure 13 shows the energy threshold as a function of the DCR, for an event occurring at around mid-chamber in configuration B (Teflon-lined TPC), and different photosensor coverage. It clearly enables energy thresholds down to nuclear binding energies ($\sim\text{MeV}$), that are generally considered to be the lowest detection energies of interest.

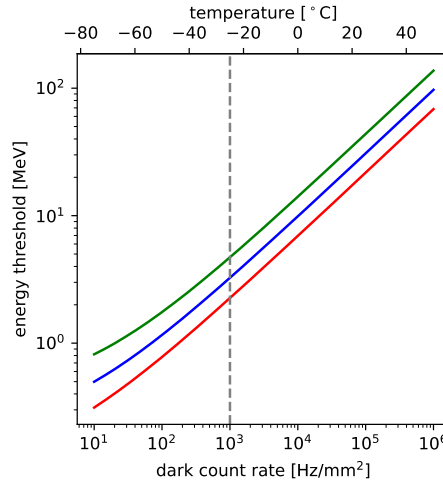


Fig. 13 Minimum event energy required to produce a detectable primary-scintillation signal ($5\text{-}\sigma$ significance), for a Teflon-lined TPC filled with Ar/ CF_4 (99/1), as a function of the SiPM DCR (bottom axis) and the corresponding operating temperature of the SiPM plane (top axis). For reference, a point-like event at about mid-chamber has been considered. The three lines correspond, respectively, to 76% (red), 38% (blue) and 19% (green) sensor coverage of the anode plane.

On the other hand, the time response of the TPC results from the time profile of the gas scintillation (Fig. 14, top-left panel) coupled to the distribution of arrival times at the photosensor including all reflections. Geant4-simulated time profiles for point-like energy deposits are shown in Fig. 14 for the configuration without reflectors (A), reflective field-cage (B) and reflective field-cage and anode (C), for different z positions of the light source within the chamber. The top-row panels show the time profiles from photon-tracing, while the bottom row shows the full TPC response including the gas scintillation profile (and arbitrarily normalized to one).

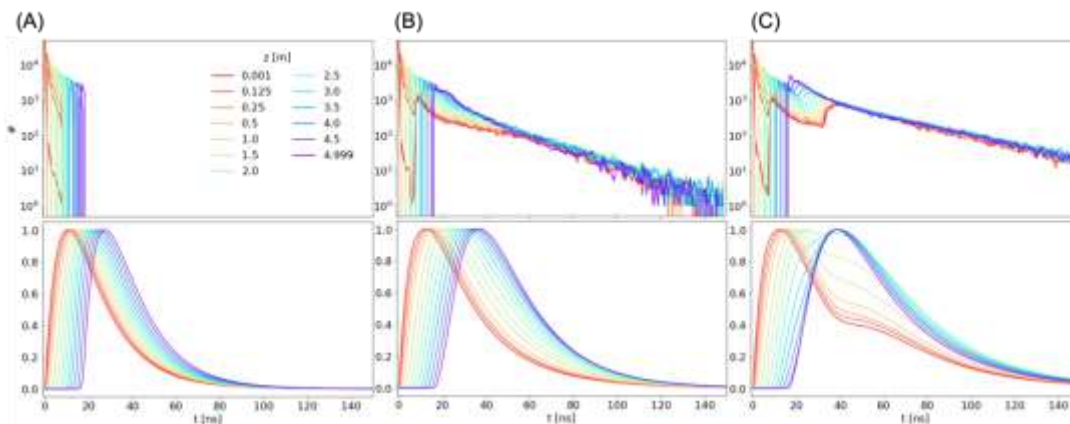


Fig. 14 Top: Geant4 simulation of the photon arrival times for 5 MeV protons in the three reference configurations discussed in the main text. The contribution from the photons reflected from the field cage and anode appear distinctly separated in case C up to about mid-chamber. Bottom: same simulation but including the gas scintillation response. Pulse shapes in a fully reflective TPC (last column) show a strong dependence with the position of the interaction, unlike the others.

When the matching between ionization and scintillation signals can be accomplished for an interaction inside the TPC, the time retrieved from the latter enables different capabilities, depending on the achievable resolution: (i) performing spill-association, (ii) z-determination (\sim cm/us -scale in gas) and (iii) vertex assignment of neutral events (expectedly, the shortest time scale of practical use). In particular, studies made by the DUNE collaboration indicate that neutrons from neutral-current interactions can be well assigned to the interaction vertex if their time-of-flight can be measured to ns accuracy. Figure 15 presents the time resolution as a function of the DCR (bottom axis), and the corresponding operating temperature of the SiPMs (top axis), for the three configurations discussed. The study has been done for point-like deposits of \approx 5 MeV (a bit above the energy threshold estimated in previous sections). The dashed vertical line indicates the proposed operating temperature (-25° C).

It can be noted that, from the point of view of the time resolution, the addition of a reflector at the anode is of little advantage as the anode-reflected light contributes little to timing except for events close to the anode (red line). When using reflectors, time resolution is situated in the range 1-2.5 ns at -25° C, whereas obtaining a comparable performance in the absence of them would require operation close to -65° C. An improvement of about a factor of 2 can be obtained with operation at a temperature of -50° C in configurations B and C (centre and right panels in Fig. 15) a performance that cannot be matched in the absence of reflectors no matter the operating temperature (left plot in Fig. 15).

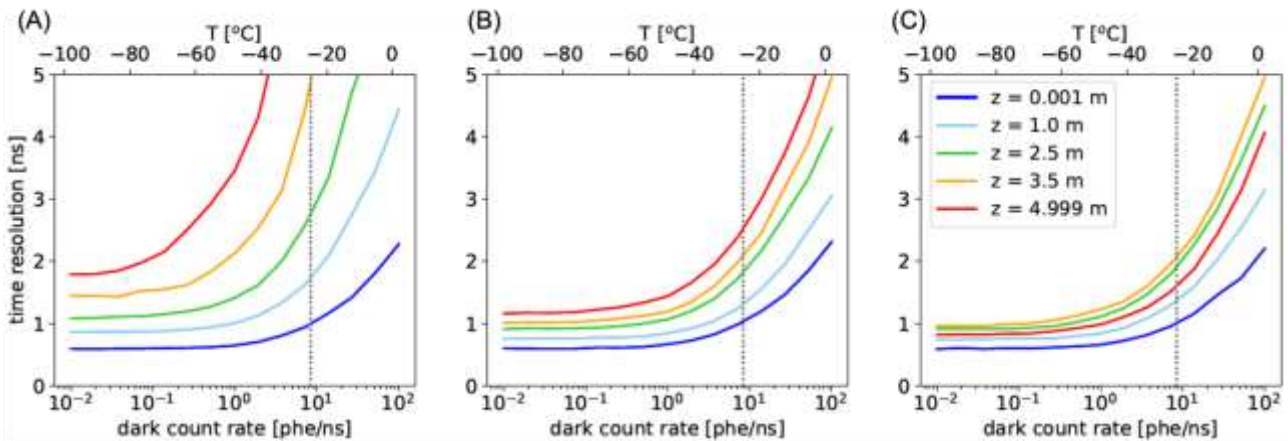


Fig. 15 Time resolution for the reconstruction of the scintillation pulse in Ar/CF₄ gas (99/1) at 10 bar, in the 5 m-diameter/5 m-length TPC considered in this work. It is represented for 5 MeV deposits as a function of DCR (lower axis) and temperature of the SiPM plane (upper axis), considering different distances (z) to the photosensor plane and for three TPC configurations: (A) TPC with no reflectors; (B) with Teflon reflector along the drift wall; (C) with Teflon reflector along the drift wall and aluminized GEMs.

3. TECHNOLOGICAL ASSETS

3.1 ACTIVE SIPM GANGING

The photosensor response function (PRF), signal-to-electronic-noise (S/N_{elec}) and sampling time (ΔT) can modify the performance presented in the previous section. In order to address their impact, we consider light pulses from a canonical 5 MeV deposit in configuration B (Teflon-lined TPC) as before, this time at a position close to the cathode (blue line in Fig. 15), to set the time resolution scale to around 1 ns. Extending over previous analysis, the PRF is now introduced as a convolution over the Geant4-generated pulses, and the waveform template used for the fit includes the convolution with the PRF as well. The decision to benchmark pulse-reconstruction through the timing

performance is partly arbitrary, however based on the observation that preserving time resolution preserves energy resolution and energy thresholds too.

We envisage SiPM ‘ganging’ in order to cover, in an affordable manner, an area of at least 7.5 m² (38% coverage). The PRF will depend on the parameters of the feedback and zero-pole cancellation loops of the amplifying electronics, and the equivalent SiPM-capacitance at its input. We consider response functions that can be realistically obtained when ganging 16 channels, as per an ongoing design based on LTSpice, including the ‘Corsi parameters’ for model S14161-6050HS (Hamamatsu), following parallel passive ganging (x 4) and active summing (x 4). The 1" photosensor footprint anticipates a lump sum of 12000 readout channels.

In simulation, a bi-exponential function allows a good description of the PRF, with two extreme cases being considered in the following: ‘fast’, where $t_{\text{rise}}=4.2$ ns and $t_{\text{fall}}=13.8$ ns; and ‘slow’, where $t_{\text{rise}}=10.1$ ns and $t_{\text{fall}}=60.8$ ns (defined from 10% to 90%). For illustration, Fig. 16-left provides the time resolution over a range of t_{rise} , t_{fall} values (sampled by Monte Carlo) including those two scenarios. Maximum variations stay well within a 30%. The small effect observed underlines the fact that the scintillation response of Ar/CF₄, together with the delays due to light reflections in the TPC, dominate over the electronic response in the range of PRF’s considered.

Another critical study is the determination of the optimum sampling time, that has a direct impact on the digitizing electronics, multiplexing strategy and cost. Again, as in previous section, the start time of the sampling process relative to the pulse has been randomized within a time bin, to mimic an asynchronous sampling. Fig. 16-right shows that the time resolution is preserved for a time sampling corresponding to $\Delta T \leq 7$ ns, that motivates the value of $\Delta T = 4$ ns chosen in the Geant4 simulation of previous section.

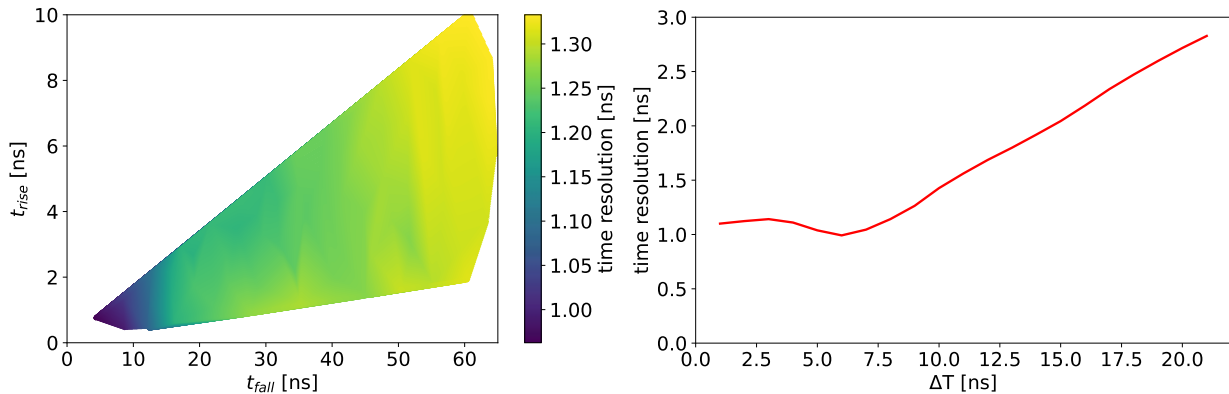


Fig. 16 Left: simulated time resolution for our reference case (5 MeV deposits) as a function of the t_{rise} and t_{fall} parameters of the photosensor impulse response (PRF), parameterized through a bi-exponential function t_{rise} and t_{fall} are defined between 10% and 90% of the signal maximum. Right: simulated time resolution for our reference case (5 MeV deposits) as a function of the time binning employed during signal digitization (‘fast’ electronics response assumed).

Finally, we evaluate the impact of the electronic noise in the pulse reconstruction. We assumed a white-noise spectrum with a normal amplitude distribution centered around 0, whose σ -value is referred to as N_{elec} . The simulated pulses are reconstructed after smearing the amplitude in each 4 ns time bin, following this noise model. The time resolution as a function of the ratio of the signal amplitude to noise (S/N_{elec}) is shown in Fig. 17. With continuous lines we present the performance when adding all electronic channels (totalling 12000 for the fill factor of 38 % discussed in text, 16-fold ganging, and assuming our 1 squared-inch baseline S14161-6050HS SiPM-sensor). With discontinuous lines we show the result of adding only channels that fired at a particular time.

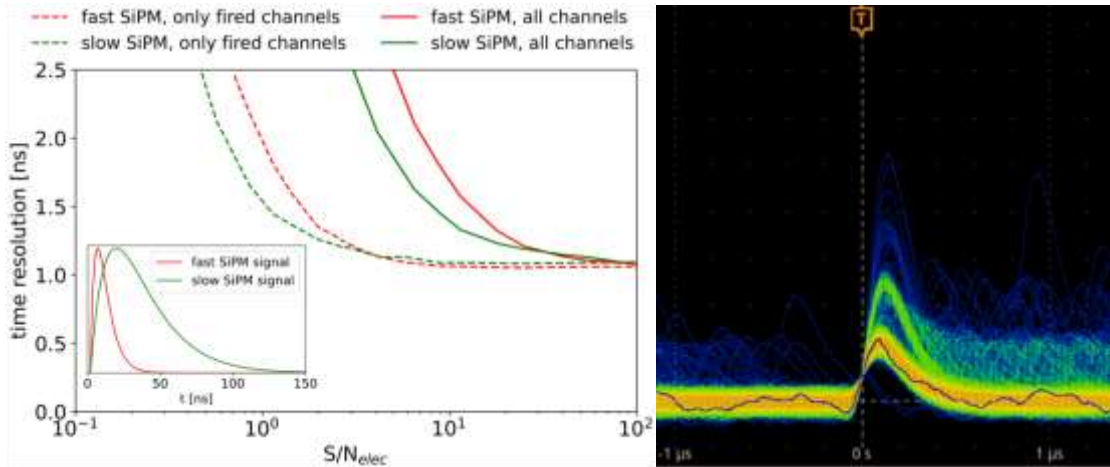


Fig. 17 Left: simulated time resolution for our reference case (5 MeV deposits) as a function of the amplitude of the signal over the electronic noise (S/N_{elec}). The inset shows the two electronic responses studied ('fast' and 'slow'). Right: oscillogram taken in persistency mode, showing preliminary results for single and double photon SiPM peaks at -25°C , obtained in a development board. The photo-sensor type and ganging scheme, as well as the width of the PRF and S/N_{elec} are compatible with those discussed in text.

As the dark-rate occupancy in a 100 ns window is only about 6%/channel at -25°C , single-photon reconstruction should remain largely unbiased, and a threshold may be in principle applied to every channel to select only those that fired in the given time window, if signal-to-noise allows. A signal-to-noise ratio around 5-10 should easily allow single-photon detection with a threshold of $3-5\sigma$ above the noise level and, according to Fig. 17-left, it should also keep the pulse-reconstruction (time resolution) of 5 MeV deposits largely unaffected (dashed lines). This seems well within reach of current technology as signal-to-noise ratios above 10 have been reported on areas similar to the ones discussed here [21]. In case of incoherently adding all channels, on the other hand, a signal-to-noise value as high as 50 would be in principle needed to maintain good reconstruction down to 5 MeV energies (continuous lines in Fig. 17-left), that seems extremely challenging. Clearly, any form of common-mode noise should be suppressed, and differential or pseudo-differential readouts seem a must at the proposed scale. Fig. 17-right shows, for illustration, preliminary results obtained in conditions comparable to the ones discussed in text, for the same photo-sensor type and a x 4 (passive) ganging. An oscillogram of the dark rate pulses in persistency mode is presented, with the single, double and triple photon peaks being clearly visible. Only one of the two legs of the pseudo-differential outputs of the board under development at IFIC has been read out.

3.2 ACTIVE CRYOSTAT

A temperature of -25°C is not alien to the operation of silicon-based photosensors [22] and, with due precautions, it is high enough not to expect strong tin pest effects on the auxiliary electronic boards. Although several cooling strategies are possible, we briefly discuss a simple implementation that avoids the use of large vacuum vessels, and that might be practical when targeting operation near a pressurized system, at a modest power consumption. Given the necessity to avoid temperature gradients in the TPC, a combination of passive insulation and a mild active heating of the external window surface is proposed. Passive insulation could be enabled by 5 mm of pressurized Ar gas and a 20 mm-thick PMMA window, coated with an Indium-Tin-Oxide (ITO) conductive film on its external surface, as shown in Fig. 18 (top). The presence of a second PMMA window at the cathode plane ensures a buffer gas region for homogenization of residual temperature gradients over the windows. Fig. 18 (bottom) shows the experimental results for a 10 cm diameter cryostat designed according to these principles cooled down to -20°C through an ethanol chiller. Upon applying a

voltage across the ITO film ($\approx 12V$), marked with an arrow as ‘ITO on’, the internal cooling power can be balanced and the system returned to stationary conditions, with a power consumption of about $100 W/m^2$. Over the entire photosensor region, this would amount to a modest $750 W$ (to which the electronics power needs to be added). The stationary values of the temperatures as well as the power per unit area are well matched in a 1D simulation. A detailed study is currently underway in order to model the temperature profile over the window, outside the axial region (Fig. 19).

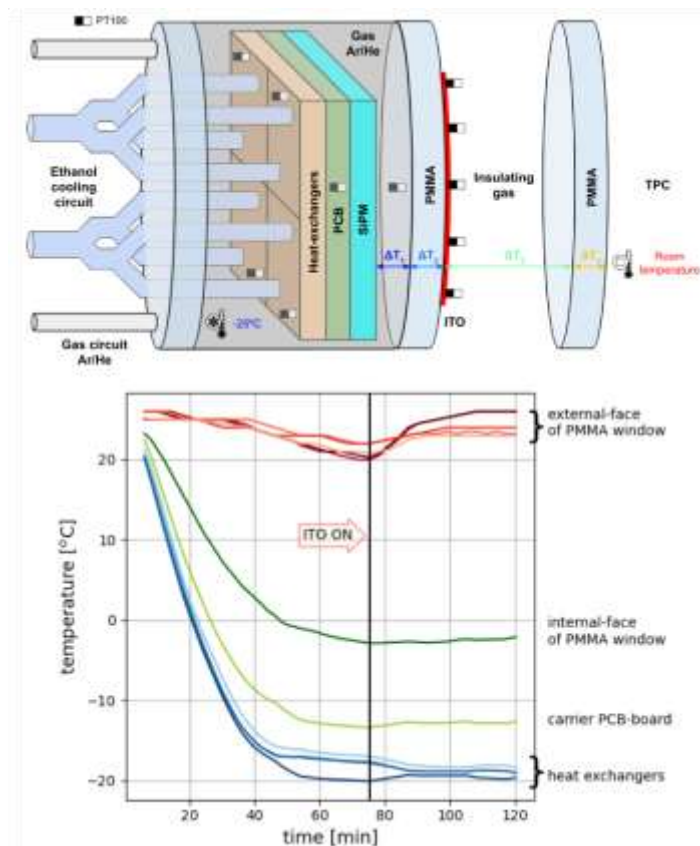


Fig. 18 A possible concept for a non-vacuum-based cryostat, relying on passive insulation and a mild external heating worth $100 W/m^2$. Bottom: experimental results, illustrating the effect of the external heating at stabilizing the external temperature. Heating was activated at the time marked with the arrow ‘ITO on’. (The carrier board had neither through-vias nor thermal pads in this test)

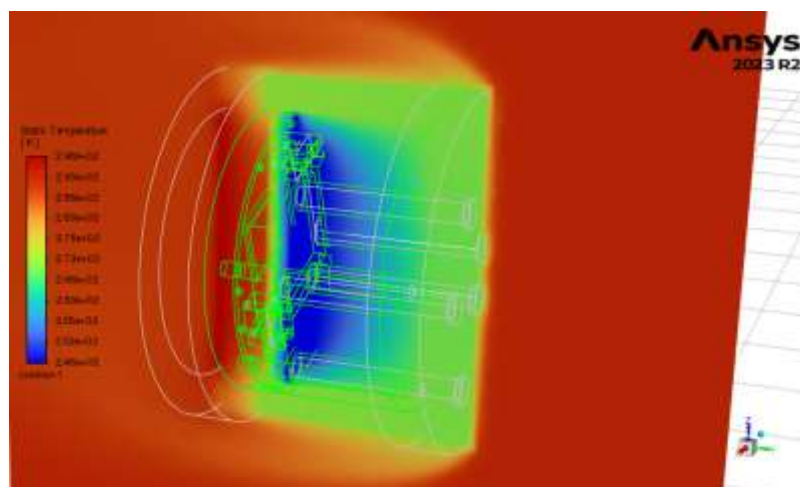


Fig. 19 ANSYS simulations showing the temperature map. A detailed comparison of the temperature profiles at the cryostat window, in data and simulations, is ongoing (courtesy of J. Collazo, UVigo).

3.3 IMPACT OF TEFLON REFLECTOR ON TPC PERFORMANCE

The use of a Teflon reflector is an important aspect of the above proposal. Although the approach is standard in the field of Rare Event searches, it requires several modifications to make it amenable to mid/high particle rates and in particular to a tracking environment, where the drift velocity needs to be stable throughout the measurements. First, the metallic electrodes (constituting the field shapers) should remain exposed, to avoid charging up of the plastics during measurements. Second, gas distribution needs to be optimized in order to efficiently remove the considerable outgassing of Teflon down to tolerable levels, in a reasonable time. The results from this work are in the final publication stage and here we just show the main conclusions, for illustration.

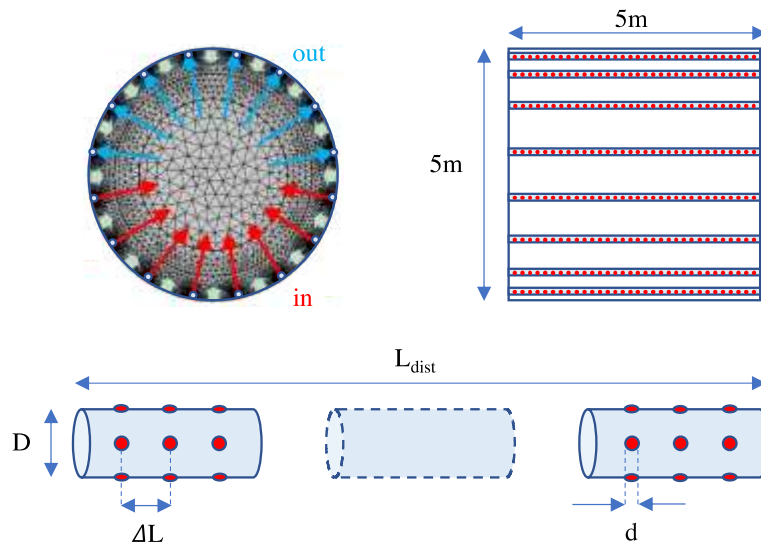


Fig. 20 Proposed gas distribution, with perforated distribution rods extending axially along the TPC (right). Eight injection rods are placed at the bottom and eight ejection rods at the top (left). The reference vessel considered in this work is 5m in length and 5m in diameter. Holes are indicated by circles (not to scale). Bottom: close-up of a gas distributor rod.

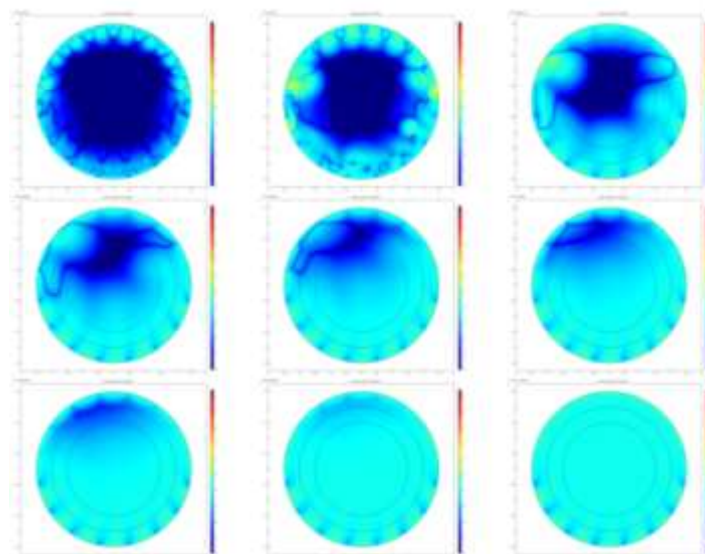


Fig. 21 Time lapse of the distribution of O_2 concentration in the cross section of our reference 10 bar argon TPC (for conditions of 'realistic' outgassing and 'realistic' flow). The two concentric circles mark the limits of the different mesh regions. The transient phase of the flow can be observed mostly in the first 6-7 images. After that, the system approaches steady state, and the concentration becomes homogeneous in the chamber.

Fig. 20 presents the proposed gas distribution and distributor geometry, based on existing literature and state-of-the-art compressors (for gas recirculation), we set for ‘realistic’ values of around $6.5 \text{ m}^3/\text{h}$ (at 10 bar) for the gas flow and $10^{-8} \text{ mbar}\cdot\text{l}/\text{cm}^2\cdot\text{s}$ for the outgassing rate. Fig. 21 shows a 2D map of the impurities as a function of time and Fig. 22 shows the performance of the proposed distributor scheme compared to other alternatives. In a bit over 1 day, the O_2 concentration stabilizes around 0.3 ppm, corresponding to a 10% charge drop due to attachment, over a 5m-drift, in 10 bar argon-based mixture at around $40 \text{ kV}/\text{cm}$. The simulation represents an upper limit, as outgassing rate is expected to decrease with time.

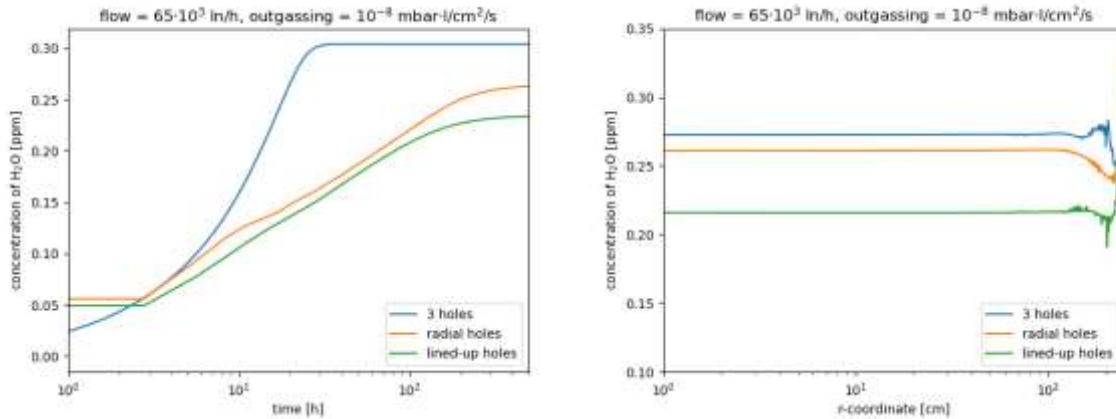


Fig. 22 Oxygen concentration simulated up to 500 h in our reference 10 bar argon TPC (*the y-axis wrongly states H_2O), at a gas flow rate of $65\cdot 10^3 \text{ l}/\text{h}$ and an outgassing rate of $10^{-8} \text{ mbar}\cdot\text{l}/\text{cm}^2\cdot\text{s}$ for three different distributor geometries. Left: evolution of the total O_2 concentration with time. Right: radial distribution of O_2 at the 500 h mark, with all distributor geometries displaying a mostly homogeneous contaminant distribution.

4. CONCLUSIONS AND OUTLOOK

The results presented establish, beyond doubt, the possibility of doing simultaneously time-tagging and accurate particle tracking in next-generation neutrino experiments, by resorting to gas scintillation. This has been demonstrated for argon-based chambers (TPCs) at 10 bar, upon the addition of a small amount of CF_4 , that acts as a gaseous wavelength-shifter. The main microscopic properties of the gas mixture, the Pyboltz and Geant4 simulations backing its use for next-generation TPCs have been presented. The necessary, and novel, assets to enable detection, are being assessed and no bottleneck is currently anticipated based on ongoing results: (i) SiPM active ganging, (ii) a cryostat based on a combination of passive insulation and active reheating, (iii) use of Teflon reflectors.

A natural extension of this work has been the possibility of accomplishing the optical imaging of the particle tracks too. Encouraging results have been obtained at 1 and 1.5 bar with a double-stack of glass-GEMs. The consortium currently focuses on the operation of a Full3D optical-TPC demonstrator at 5-10 bar, read out with TimePix cameras (for tracking) and SiPM tiles (for the T_0 signal), and is currently under commissioning. It will be used to demonstrate the performance of the above technological assets in a realistic system and will be briefly discussed during the AIDAInnova meeting.

5. REFERENCES

- [1] C. Andreopoulos et al., ‘Proposal to Measure Hadron Scattering with a Gaseous High Pressure TPC for Neutrino Oscillation Measurements’, *Tech. Rep. CERN-SPSC-2017-030, SPSC-P-355, CERN, Geneva (2017)*.
- [2] DUNE collaboration, ‘A Gaseous Argon-Based Near Detector to Enhance the Physics Capabilities of DUNE’, *arXiv: 2203.06281*.
- [3] C. Cantini et al., ‘Performance study of the effective gain of the double phase liquid Argon LEM Time Projection Chamber’, *JINST 10 (2015) P03017, arXiv: 1412.4402*.
- [4] A. Tesi, S. Leardini et al., ‘The cryogenic RWELL: a stable charge multiplier for dual-phase liquid argon detectors’, *Eur. Phys. J. C 83 (2023) 979*.
- [5] L. Olano-Vegas, I. Pardo, S. Leardini, M. Morales et al., ‘Development of Fe₂O₃/YSZ ceramic plates for cryogenic operation of resistive-protected gaseous detectors’, *Front. Detect. Sci. Technol. 1 (2023) 1234229*.
- [6] R. Santorelli, E. Sanchez Garcia, P.G. Abia, D. González-Díaz, R.L. Manzano, J.J.M. Morales et al., ‘Spectroscopic analysis of the gaseous argon scintillation with a wavelength sensitive particle detector’, *Eur. Phys. J. C 81 (2021) 622, arXiv: 2012.08262*.
- [7] P. Amedo, D. González-Díaz, F.M. Brunbauer, D.J. Fernández-Posada, E. Oliveri and L. Ropelewski, ‘Observation of strong wavelength-shifting in the argon-tetrafluoromethane System’, *Front. Detect. Sci. Technol. 1 (2023) 1282854, arXiv: 2306.09919*.
- [8] P. Amedo, S. Leardini, A. Saá-Hernández and D. González-Díaz, ‘Primary scintillation yields induced by α particles in gas mixtures of Argon/CF₄ at 10 bar’, (in preparation).
- [9] M. Deptuch and T.Z. Kowalski, ‘Gas multiplication process in mixtures based on Ar, CO₂, CF₄’, *Nucl. Instrum. Meth. A 572 (2007) 184*.
- [10] C. Bault, A. Beschi, F. Brunbauer, D. González-Díaz, H. Muller, E. Oliveri et al., ‘A survey on GEM-based readouts and gas mixtures for optical TPCs’, in the 14th Vienna Conference on Instrumentation (VCI2016), 2016, <https://indico.cern.ch/event/391665/contributions/1827205/>.
- [11] F.M. Brunbauer, G. Galgóczi, D. Gonzalez Diaz, E. Oliveri, F. Resnati, L. Ropelewski et al., ‘Live event reconstruction in an optically read out GEM-based TPC’, *Nucl. Instrum. Meth. A 886 (2018) 24*.
- [12] F.M. Brunbauer, F. Garcia, T. Korkalainen, A. Lugstein, M. Lupberger, E. Oliveri et al., ‘Combined optical and electronic readout for event reconstruction in a GEM-based TPC’, *IEEE Trans. Nucl. Sci. 65 (2018) 913*.
- [13] F.M. Brunbauer, M. Lupberger, E. Oliveri, F. Resnati, L. Ropelewski, C. Strelt et al., ‘Radiation imaging with optically read out GEM-based detectors’, *JINST 13 (2018) T02006*.
- [14] P. Amedo, R. Hafeji, A. Roberts, A. Lowe, S. Ravinthiran, S. Leardini et al., ‘Scintillation of Ar/CF₄ mixtures: glass-THGEM characterization with 1% CF₄ at 1-1.5 bar’, submitted to *JINST (2023) [arXiv:2312.07503]*.
- [15] L. Margato, A. Morozov, L. Pereira, M. Fraga and F. Fraga, ‘Effect of the gas contamination on CF₄ primary and secondary scintillation’, *Nucl. Instr. Meth. A 695 (2012) 425*.

-
- [16] B. Al Atoum, S.F. Biagi, D. González-Díaz, B.J.P. Jones and A.D. McDonald, ‘Electron transport in gaseous detectors with a Python-based Monte Carlo simulation code’, *Comput. Phys. Commun.* 254 (2020) 107357 [1910.06983].
- [17] S. Leardini et al., ‘Time and band-resolved scintillation in time projection chambers based on gaseous xenon’, *Eur. Phys. Journal C*, 82, 425(2022).
- [18] E. Robert, A. Khacef, C. Cachoncille, J.M. Pouvesle, ‘Time-resolved spectroscopy of high pressure rare gases excited by an energetic flash X-ray source’, *Optics Communications*, 117(1995) 179-188.
- [19] A. Morozov et al., ‘Photon yield for ultraviolet and visible emission from CF₄ excited with alpha particles’, *Nuclear Instruments and Methods in Physics Research, Section B: Beam Interactions with Materials and Atoms* 268(9) (2010) 1456–1459.
- [20] A. Saá-Hernández, D. González-Díaz, et al., ‘On the determination of the interaction time of GeV neutrinos in large argon gas TPCs’, *arXiv: 2401.09920*.
- [21] M. D’Incecco, C. Galbiati, G.K. Giovanetti, G. Korga, X. Li, A. Mandarano et al., ‘Development of a Novel Single-Channel, 24 cm², SiPM-Based, Cryogenic Photodetector’, *IEEE Trans. Nucl. Sci.* 65 (2017) 591, *arXiv: 1706.04220*.
- [22] PANDA collaboration, Technical Design Report for PANDA Electromagnetic Calorimeter (EMC), *arXiv: 0810.1216*